ADVANCED FUNCTIONAL MATERIALS
www.afm-journal.de

Materials Views
www.MaterialsViews.com

Hierarchical NiMn Layered Double Hydroxide/Carbon Nanotubes Architecture with Superb Energy Density for Flexible Supercapacitors

Jingwen Zhao, Jiale Chen, Simin Xu, Mingfei Shao, Qiang Zhang, Fei Wei, Jing Ma, Min Wei, David G. Evans, and Xue Duan*

A hierarchical nanostructure composed of NiMn-layered double hydroxide (NiMn-LDH) microcrystals grafted on carbon nanotube (CNT) backbone is constructed by an in situ growth route, which exhibits superior supercapacitive performance. The resulting composite material (NiMn-LDH/CNT) displays a three-dimensional architecture with tunable Ni/Mn ratio, well-defined core-shell configuration, and enlarged surface area. An electrochemical investigation shows that the Ni_3Mn_1-LDH/CNT electrode is rather active, which delivers a maximum specific capacitance of 2960 F g^{-1} (at 1.5 A g^{-1}), excellent rate capability (79.5% retention at 30 A g^{-1}), and cyclic stability. Moreover, an all-solid-state asymmetric supercapacitor (SC) with good flexibility is fabricated by using the NiMn-LDH/CNT film and reduced graphene oxide (RGO)/CNT film as the positive and negative electrode, respectively, exhibiting a wide cell voltage of 1.7 V and largely enhanced energy density up to 88.3 Wh kg^{-1} (based on the total weight of the device). By virtue of the high-capacity of pseudocapacitive hydroxides and desirable conductivity of carbon-based materials, the monolithic design demonstrated in this work provides a promising approach for the development of flexible energy storage systems.

1. Introduction

In the last decade, portable/wearable personal electronics have attracted extensive attention because of their high flexibility, foldability and conformability, which poses challenges for the design and fabrication of compatible energy conversion and storage devices.[1–3] The emerging flexible solid-state supercapacitors (SCs) normally combine the large power density and super-high cycle life with remarkable mechanical properties, and hence play a key role in the future electrical energy storage field.[4–6] The realization of high-performance flexible SCs strongly relies on the electrical properties and mechanical integrity of the constitutive materials and their ingenious assembly into free-standing and binderless skeleton.[7–9] Recent advances in flexible miniature devices have been driven by highly-conductive and robust materials such as stretchable carbon nanotubes (CNTs) or graphene thin films, elastic bucky gels and other polymer/carbon composites.[10–16] Despite the great progress made recently, the intrinsic limitation of the electrostatic surface charging mechanism and the agglomeration of polymers tend to result in relatively low capacitance; moreover, current flexible SCs still suffer from relatively poor energy output in comparison with lithium ion batteries. These drawbacks would impede their further development in the key enabling technologies including emergency power systems and portable power tools.

Pseudocapacitive metal (e.g., ruthenium, nickel, cobalt and manganese) hydroxides/oxides provide multiple oxidation states for reversible Faradaic reactions; the incorporation of pseudocapacitive species with carbon-based materials has been extensively pursued to realize efficient SC devices.[17–21] These composites are believed to compensate for intrinsic carrier transportation resistance of metal hydroxides/oxides and, in the mean time, to boost the whole energy density.[7,22,23] In most cases, however, the weak contact between carbon materials and pseudocapacitive species may lead to sluggish kinetics for charge separation, which in turn hinders the possible synergistic effect between individual constituents. Additionally, the capacitance degradation due to the dramatic volume change over charge-discharge cycling is still a great challenge in achieving durable solid-state SCs. Recently, considerable interest has been focused on metal oxide-based pseudocapacitors with well-defined three-dimensional (3D) configuration, especially the core-branched structures, in which highways of both electrolyte and electron are simultaneously constructed to

J. Zhao, J. Chen, S. Xu, M. Shao, Prof. M. Wei, Prof. D. G. Evans, Prof. X. Duan
State Key Laboratory of Chemical Resource Engineering
Beijing University of Chemical Technology
Beijing 100029, P. R. China
E-mail: weimin@mail.buct.edu.cn
Dr. Q. Zhang, Prof. F. Wei
Beijing Key Laboratory of Green Chemical Reaction Engineering and Technology
Department of Chemical Engineering
Tsinghua University
Beijing 100084, P. R. China
Prof. J. Ma
School of Chemistry and Chemical engineering
Nanjing University
Nanjing 210093, P.R. China

DOI: 10.1002/adfm.201303638

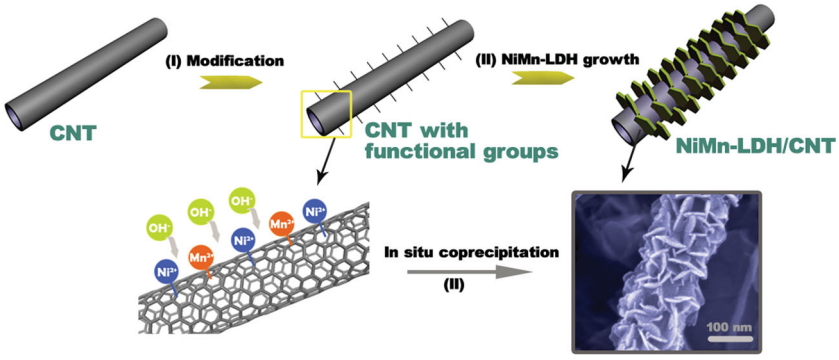

Scheme 1. Schematic illustration for the synthesis and morphology of NiMn-LDH/CNT. Step (I): the surface modification of CNT by functional groups (e.g., $-OH^-$, –CO, $-COO^-$). Step (II): the grafting of NiMn-LDH nanosheets onto CNT backbone by an in situ growth method.

facilitate efficient energy storage at high rates.[20,23,24] Therefore, one effective approach to resolve the above problems is to build up an integrated hierarchical architecture via self-assembling electroactive materials onto specific carbon backbones firmly, in which structural features of each component are thoroughly presented to guarantee sufficient exposure of active sites, fast ion/electron transport and hence to realize the full potential of the composite materials.

It is known that monometallic oxides/hydroxides (e.g., $Ni(OH)_2$ and $Co(OH)_2$) generally suffer from low durability owing to severe transformation between polymorphic forms.[25–27] A great deal of research has been therefore devoted to seeking their bimetallic counterparts with stable structural characteristics.[28–31] Layered double hydroxides (LDHs) are a family of inorganic multi-metal clay materials, whose structure is based on positively-charged brucite-like layers and interlayer charge compensating anions.[32–36] Recently, transition metal-based LDHs materials have attracted much attention in electrochemical sensors, electrocatalysts and SCs, owing to their low cost, high stability and versatility in both composition and morphology.[37–41] Herein, we designed and fabricated a sophisticated hierarchical architecture composed of high-quality NiMn-LDH nanosheets anchored on the CNT backbone (denoted as NiMn-LDH/CNT), and demonstrated its excellent behavior in high-performance flexible SCs. In view of this monolithic design, the NiMn-LDH/CNT electrode yields largely improved capacitance (2960 F g^{-1} at 1.5 A g^{-1}), while maintaining remarkable rate capability and long cycling life. The NiMn-LDH nanosheets with large surface area ensure a sufficient pseudocapacitive reaction; while the CNT backbone serves as a conductive and robust network to facilitate the electron collection/transport, and simultaneously buffers the large volume change of active species in long-term cycling. In addition, an all-solid-state asymmetric supercapacitor (SC) with good flexibility was fabricated based on the NiMn-LDH/CNT film electrode, which manifests an energy density up to 88.3 Wh/kg as well as long-term stability, outperforming most currently available flexible SCs.

2. Results and Discussion

2.1. Structural and Morphological Study of the NiMn-LDH/CNT

The fabrication process of NiMn-LDH/CNT is displayed in **Scheme 1**. CNTs are an important one-dimensional nanomaterial with a huge aspect ratio and an unique combination of mechanical, electrical, and thermal property. Representative SEM images of the CNTs reveal an entangled network consisting of numerous individual nanotube with the diameter of ≈35 nm and length up to micrometer scale (**Figure 1**a and the inset). A conventional acid treatment of CNTs was performed, so as to introduce functional groups (e.g., hydroxyl, carbonyl, and carboxyl) (Scheme 1: Step I), which not only facilitate the dispersion of CNTs but also serve as nucleation centers for the deposition of NiMn-LDH. Through a facile in situ growth method (Scheme 1: Step II), an uniform coating of NiMn-LDH nanosheets with high density was produced on the skeleton of CNTs, with an open and porous structure (Figure 1b). The resulting single NiMn-LDH/CNT (diameter: ≈250 nm) is composed of dozens of interconnected sheet-like subunits (Figure 1c). The unique NiMn-LDH/CNT core-shell heterostructure is evidenced by TEM images (Figure 1d,e), in which the gauze-like NiMn-LDH nanosheets are densely grafted throughout the longitudinal axis of the nanotube. The XRD pattern of NiMn-LDH/CNT can be indexed to a rhombohedral LDH phase with the interbrucite-like sheet distances (d_{003}) of 7.75 Å, in accordance with the powdered sample for

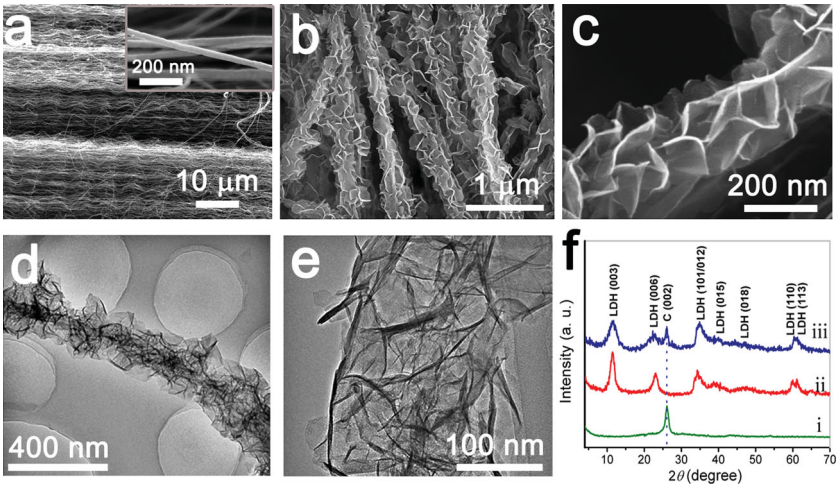

Figure 1. a) SEM image of the pristine CNT (inset: the enlarged image). b,c) SEM images and d,e) TEM images of the NiMn-LDH/CNT. f) XRD patterns of: i) the pristine CNT, ii) the powdered sample of NiMn-LDH, iii) the NiMn-LDH/CNT.

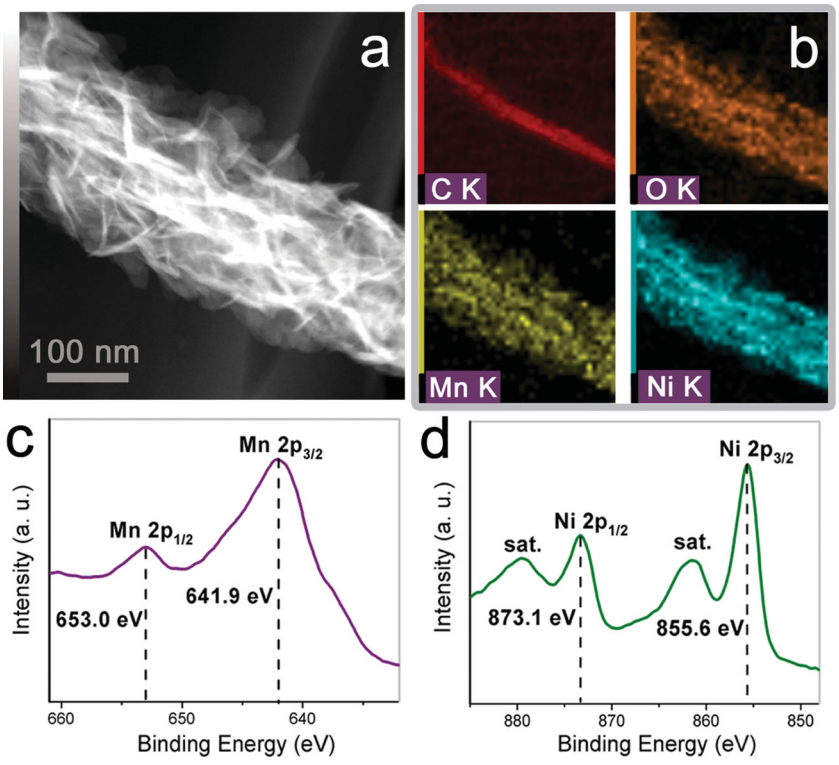

Figure 2. a) HADDF-STEM image and b) EDS mapping of C, O, Mn, and Ni element on an individual NiMn-LDH/CNT core-shell nanostructure; XPS spectra of c) Mn 2p and d) Ni 2p of the NiMn-LDH/CNT composite.

comparison (Figure 1f). The peak at 26.3° ascribed to the (002) plane of hexagonal graphite structure indicates the presence of CNTs.[42] No other crystalline phase was detected, indicating the high purity of the final product. The selected area electron diffraction (SAED) analysis (Figure S1, Supporting Information) is superimposed by the diffraction rings from polycrystalline NiMn-LDH nanosheets and a pair of short arc from (002) diffraction of CNTs, indicating the assembly of NiMn-LDH nanosheets onto CNT backbone. The HRTEM image further verifies the close integration of NiMn-LDH and CNT (Figure S2, Supporting Information).

The Raman spectrum of the NiMn-LDH/CNT composite material is shown in Figure S3. In addition to the three peaks from CNTs (D band at 1345 cm^{-1}, G band at 1585 cm^{-1} and D" band at 2690 cm^{-1}),[43] the peaks observed at 456 cm^{-1}, 537 cm^{-1} (Metal–Oxygen–Metal bonds), and 1059 cm^{-1} (the interlayer CO_3^{2-}) demonstrate the successful introduction of the LDH phase.[44] It is noteworthy that the value of R ($R = I_D/I_G$) is used to evaluate the degree of graphitization of carbon materials.[45] Correspondingly, the calculated R value increases from 0.37 for pristine CNTs to 0.46 for the NiMn-LDH/CNT, indicative of more structural defects of CNTs in the composite. This is related to the anchoring of LDH nanosheets onto the surface of CNTs via some chemical bonds.[43] The typical high-angle annular dark-field scanning TEM (HAADF-STEM) image of an individual NiMn-LDH/CNT nanostructure and corresponding energy-dispersive X-ray spectrometry (EDS) mapping analysis (**Figure 2**a,b) unambiguously confirm the well-defined NiMn-LDH shell/CNT core hierarchical structure with the homogeneous distribution of both Mn and Ni throughout the outer shell. The mapping result is consistent with the EDS line scanning (Figure S4, Supporting Information), in which the Ni/Mn molar ratio was found to be ≈3.0. X-ray photoelectron spectroscopy (XPS) was used to characterize valence state of the obtained material, as presented in Figure 2c,d. The Mn $2p_{3/2}$ and Mn $2p_{1/2}$ peaks are located at ≈641.9 and ≈653.0 eV, suggesting the presence of Mn^{3+} in the sample.[46] The Ni $2p_{3/2}$ (855.6 eV) and Ni $2p_{1/2}$ (873.17 eV) peak accompanied with two satellite bands indicate the existence of Ni^{2+} state.[46]

The surface area and pore-size distribution are two key factors for the electroactive materials in electrical storage applications. Therefore, the N_2-adsorption/desorption measurements were carried out to study the surface area and porosity property of NiMn-LDH/CNT composite, with pristine CNT, powdered NiMn-LDH and $Ni(OH)_2$/CNT as reference samples (**Figure 3**). Typical IV isotherms with H3-type hysteresis loops ($P/P_0 > 0.4$) are observed for the NiMn-LDH/CNT and $Ni(OH)_2$/CNT, indicating the presence of a mesoporous structure. This type of hysteresis loops does not exhibit any limiting adsorption at high P/P_0 region, which is commonly attributed to particle aggregates with slit-shaped pores. From the pore size distributions (Figure 3, inset), the NiMn-LDH/CNT possesses mesopores with a relatively narrow size distribution in the range 2–10 nm. Moreover, the NiMn-LDH/CNT with the hierarchical structure exhibits a large apparent

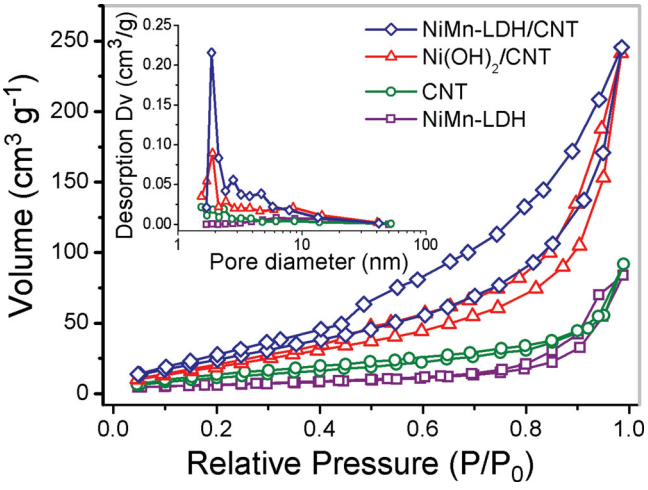

Figure 3. N_2-sorption isotherms and pore size distribution (inset) of NiMn-LDH/CNT (blue), $Ni(OH)_2$/CNT (red), pristine CNT (green) and powdered sample of NiMn-LDH (purple).

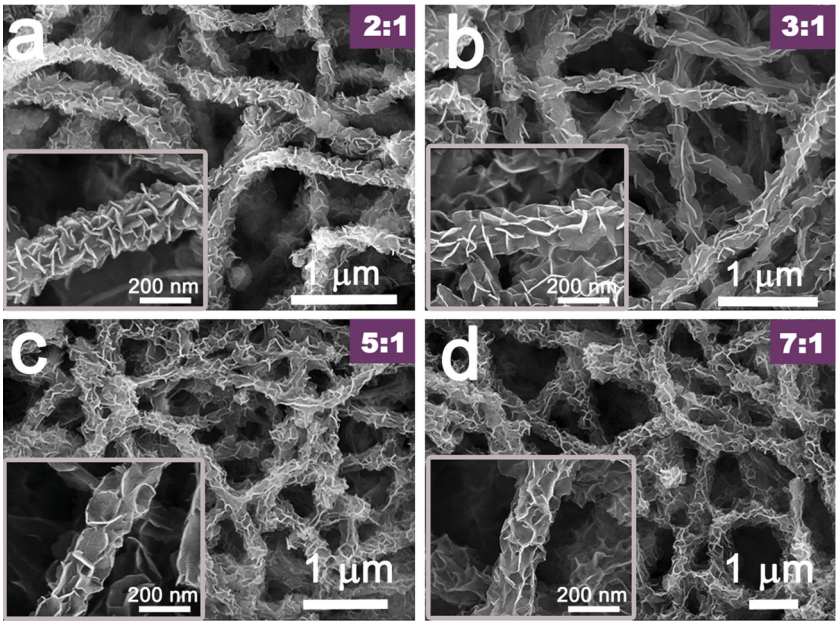

Figure 4. Typical SEM images of the Ni_xMn_1-LDH/CNT composites with various Ni/Mn ratios: a) 2:1, b) 3:1, c) 5:1, d) 7:1.

specific surface area (198 m^2 g^{-1}) and total pore volume (0.38 cm^3 g^{-1}) calculated by the Brunauer-Emmett-Teller (BET) method, which is much higher than that of the other samples (Table S1, Supporting Information). By virtue of its large surface area and the unique hierarchical porous structure, the NiMn-LDH/CNT composite material is beneficial to the kinetics of reaction and the mechanical integrity (see below).

The current synthetic strategy was extended to prepare the hierarchical structures with tunable Ni/Mn ratio. Typical SEM images of Ni_2Mn_1-LDH/CNT, Ni_3Mn_1-LDH/CNT, Ni_5Mn_1-LDH/CNT, and Ni_7Mn_1-LDH/CNT are given in **Figure 4**a–d, respectively. With the decrease of Mn content, the rigid nanosheet feature of LDH becomes indistinct, which agrees well with the decrease in the crystallinity shown in the XRD measurements (Figure S5, Supporting Information). In addition, the CoMn-LDH/CNT and $Ni(OH)_2$/CNT nanostructures were also successfully prepared via the same method (see Figure S6,S7, Supporting Information), verifying the generality and versatility of this synthetic approach. Aiming at the optimal LDH loading in the NiMn-LDH/CNT composite, the time-dependent experiments were also carried out to tune the core-shell ratio. An enhancement of both the shell thickness and density was observed upon increasing deposition time from 3 h to 36 h (Figure S8a–d, Supporting Information), indicating a stepwise and regular growth procedure. This is confirmed by the Raman spectra (Figure S8e, Supporting Information) and thermogravimetric analysis (TGA: Figure S9, Supporting Information). The value of specific capacitance shows a systematic enhancement as the deposition time increases from 3 h to 12 h; while a steep decline was observed with further increase of time (Figure S8f). Therefore, this inflection point at 12 h was chosen as the optimum condition for further study.

2.2. Electrochemical Performance of the NiMn-LDH/CNT Composites

The electrochemical behavior of hierarchical Ni_xMn_1-LDH/CNT (x = 2, 3, 5, 7) samples were investigated by cyclic voltammetry (CV) and galvanic charge-discharge in a three-electrode cell with a Hg/HgO reference electrode and 1 M KOH aqueous electrolyte. **Figure 5**a and Figure S10, Supporting Information, shows typical CV curves in a potential range 0–0.6 V at various scan rates. The redox current peaks during the anodic and cathodic sweeps were explicitly observed for each electrode, corresponding to the typical pseudocapacitive behavior of Ni^{2+}/Ni^{3+} with assistance of OH^-.[20] In comparison with the $Ni(OH)_2$/CNT (dash line in Figure 5a), the Ni_xMn_1-LDH/CNT samples ($x \leq 5$) possess larger enclosed area of CV curves, indicating that the $Mn(OH)_6$ unit plays an important role in the pseudocapacitive activity. The integrated area for Ni_xMn_1-LDH/CNT samples expands gradually with boosted gravimetric current density as x decreases from 7 to 3, while a dramatic decay in current density was observed at x = 2. The sample of Ni_3Mn_1-LDH/CNT shows the optimum electrochemical performance. To illustrate the merit of the elaborate architecture with the assistance of CNTs, we have also compared the electrochemical behavior of Ni_3Mn_1-LDH/CNT with that of the Ni_3Mn_1-LDH powdered sample (Figure S11, Supporting Information). The composite material displays both enhanced currents and depressed peak separation, demonstrating the improved utilization of the electroactive species.

The capacitive performance was further investigated with galvanostatic charge-discharge measurements (Figure 5b). On the basis of the discharge curve, the Ni_3Mn_1-LDH/CNT shows a specific capacitance as high as 2960 F g^{-1} (based on the whole sample mass) at a current density of 1.5 A g^{-1}, which is 1.8 time higher than that of the $Ni(OH)_2$/CNT (1668 F g^{-1}). The specific capacitance of these hierarchical composites at different charge-discharge current densities is shown in Figure 5c. Within the whole current density range, the Ni_3Mn_1-LDH/CNT yields substantially higher specific capacitance than that of the other samples, in line with the CV results. At a high current density of 30 A g^{-1}, 79.5% of the capacitance (from 2960 F g^{-1} to 2338 F g^{-1}) is still retained for the Ni_3Mn_1-LDH/CNT, superior to most Ni-based/carbon composites.[20,21,47] It is well-known that the stability of transition-metal hydroxides in alkaline solution is crucial in commercial alkaline batteries and pseudocapacitors. Cycling life tests were further investigated using galvanostatic charge-discharge technique at 12 A g^{-1} (Figure 5d). Interestingly, the specific capacitance increases firstly and then decays slightly for all the Ni_xMn_1-LDH/CNT samples. Compared with the $Ni(OH)_2$/CNT (6.3% loss), the Ni_xMn_1-LDH/CNT samples display better charge-discharge stability and structural integrality after 2000 cycles, with 2.8% loss for Ni_2Mn_1-LDH/CNT, 0.9% loss for Ni_3Mn_1-LDH/CNT, 2.5% loss for Ni_5Mn_1-LDH/CNT and 3.3% loss for Ni_7Mn_1-LDH/CNT, respectively. The

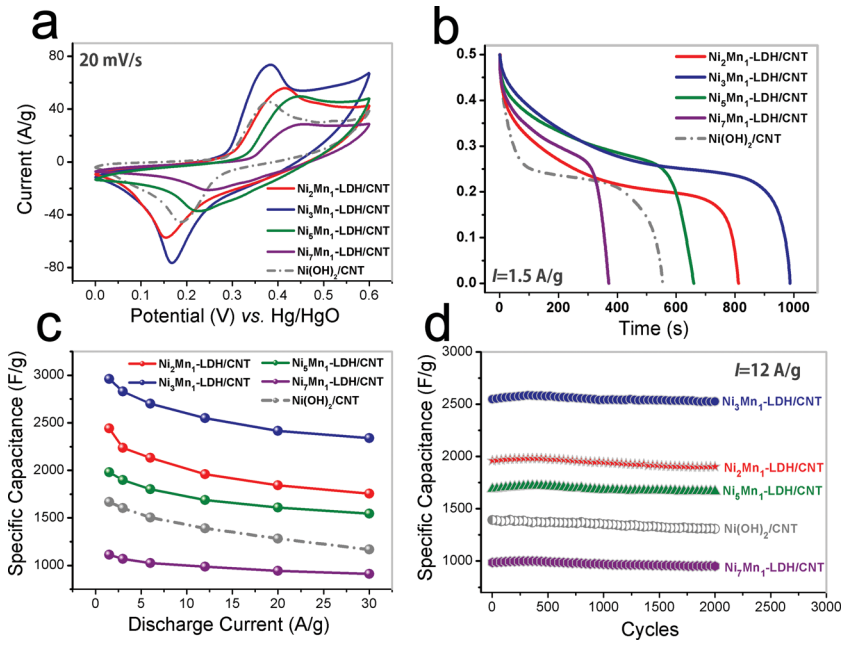

Figure 5. Electrochemical performance of Ni_xMn_1-LDH/CNT and $Ni(OH)_2$/CNT: a) CV curves, b) galvanostatic discharge curves, c) specific capacitance as a function of current density, d) cycle stability.

results highlight the capability of the Ni_xMn_1-LDH/CNT composites to meet the requirements of both long cycle lifetime and good rate capability, which are prerequisites for practical energy storage devices.

Further understanding of the LDH template stabilizing the electrochemical behavior was conducted by impedance measurements. **Figure 6** shows Nyquist plots of Ni_3Mn_1-LDH/CNT and $Ni(OH)_2$/CNT electrode, representing the characteristic depressed semicircle in the high- and medium-frequency region and extended tail in the low frequency region. According to the equivalent circuit,[48] the charge-transfer resistance (R_{CT}) for the Ni_3Mn_1-LDH/CNT was calculated to be 1.21 Ω, lower than that of the $Ni(OH)_2$/CNT (1.48 Ω). Particularly, after 2000 cycles, a slight increase in the R_{CT} is observed for the Ni_3Mn_1-LDH/CNT (from 1.21 to 1.27 Ω), while the R_{CT} of $Ni(OH)_2$/CNT increases significantly from 1.48 to 3.52 Ω, which indicates that the LDH matrix markedly enhances the cycleability of pseudocapacitive species.

Since the multi-metal LDH matrix imposes a key influence on achieving significantly high capacitive activity, density functional theory (DFT) calculations were performed to elucidate the electronic structure of Ni_xMn_1-LDHs from the theoretical viewpoint. Figure S12,S13, Supporting Information, show the optimized structures and band structure diagrams for $Ni(OH)_2$ and Ni_xMn_1-LDHs (Ni_7Mn_1-LDH, Ni_3Mn_1-LDH and $Ni_{1.67}Mn_1$-LDH), respectively. The calculated density of states (DOS: Figure S14, Supporting Information) curves indicate that the pristine $Ni(OH)_2$ possesses a typical semiconductor characteristic, whereas the spin-up states of the Ni_xMn_1-LDHs are gapless and display obviously increased local DOS values across the Fermi level, presenting a half-metallic nature. As the electron transport in the solid phase is closely related to states density of the band edge,[49] the eminently increased DOS values arising from the introduction of Mn ensure a high carrier mobility. Furthermore, the calculations reveal that the metallic feature in the spin-up DOS primarily originates from hybridization among the Ni 3d, Mn 3d, and O 2p (Figure S15, Supporting Information). In addition to the electronic structure, we also investigated the influence of Mn element on the desorption of surface hydrogen atoms, which is a critical step in the redox reaction of metal hydroxides.[50] In **Figure 7**a–d, circles a–p show that the surface adsorbed hydrogen atoms on the hydroxide layer can be divided into three kinds of local environment: Ni_3–OH, Ni_2Mn_1–OH, and Ni_1Mn_2–OH (Figure 7e–g). **Table** 1 lists the hydrogen desorption energies (E_D) and corresponding average values, from which E_D dramatically decreases along with the increase of Mn content, demonstrating the positive effect of Mn on the hydrogen desorption. It should be noted that the optimum Ni/Mn ratio in this system is found to be 3:1 with the lowest average E_D (0.439 eV for Ni_3Mn_1-LDH), which is consistent with the electrochemical data discussed above (Figure 5). By virtue of the versatility in metal cations of LDH matrix, the NiMn-LDH in this work can be regarded as "Mn-doped $Ni(OH)_2$". Since Mn species presents a mixture of several valence states, its incorporation may provide additional pathways for redox reaction and thus facilitate the overall electrochemical process. Moreover, the partial isomorphous substitution of Ni^{2+} by Mn^{3+} in the $Ni(OH)_2$ lattice to form a hydrotalcite-like structure leads

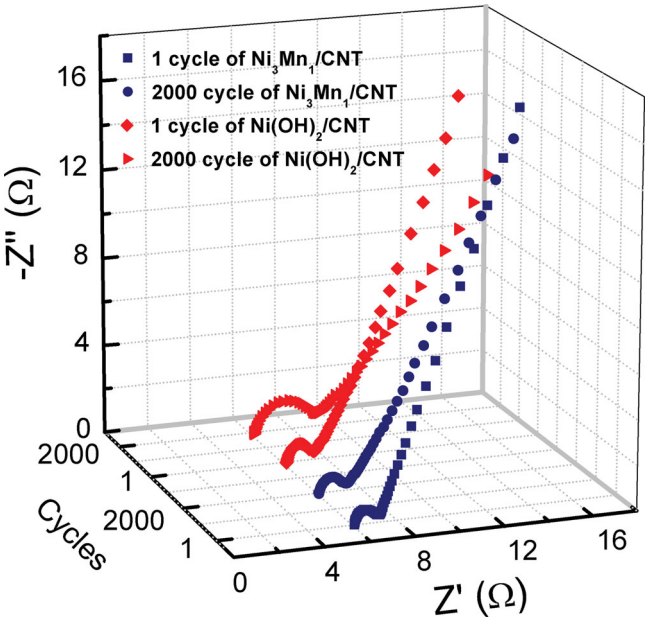

Figure 6. Nyquist plots for the 1st and 2000th charge-discharge cycle for the Ni_3Mn_1-LDH/CNT and $Ni(OH)_2$/CNT, respectively.

Table 1. Desorption energies (E_D) of hydrogen from $Ni(OH)_2$, Ni_7Mn_1-LDH, Ni_3Mn_1-LDH, and $Ni_{1.67}Mn_1$-LDH. The E_D values vary depending on the type of hydroxyl groups on the host layer (i: Ni_3–OH, ii: Ni_2Mn_1–OH, iii: Ni_1Mn_2–OH).

$Ni(OH)_2$		Ni_7Mn_1-LDH		Ni_3Mn_1-LDH		$Ni_{1.67}Mn_1$-LDH	
H atom	E_D [eV]	H atom	E_D [eV]	H atom	E_D [eV]	H atom	E_D [eV]
a^i	0.533	a^{ii}	0.492	a^{ii}	0.439	a^{ii}	0.453
b^i	0.541	b^i	0.483	b^{ii}	0.442	b^{iii}	0.440
c^i	0.548	c^i	0.502	c^{ii}	0.434	c^{ii}	0.456
d^i	0.547	d^{ii}	0.490	d^{ii}	0.436	d^{ii}	0.443
e^i	0.534	e^i	0.502	e^i	0.446	e^i	0.452
f^i	0.538	f^i	0.483	f^{ii}	0.439	f^{iii}	0.447
g^i	0.535	g^i	0.500	g^i	0.445	g^{ii}	0.438
h^i	0.540	h^i	0.488	h^{ii}	0.440	h^{ii}	0.446
i^i	0.541	i^{ii}	0.497	i^{ii}	0.439	i^{ii}	0.454
j^i	0.540	j^i	0.490	j^{ii}	0.439	j^{iii}	0.435
k^i	0.534	k^i	0.503	k^{ii}	0.434	k^{ii}	0.456
l^i	0.531	l^{ii}	0.486	l^{ii}	0.442	l^{ii}	0.447
m^i	0.545	m^i	0.500	m^i	0.435	m^i	0.464
n^i	0.542	n^i	0.497	n^{ii}	0.440	n^{iii}	0.443
o^i	0.543	o^i	0.484	o^i	0.439	o^{ii}	0.444
p^i	0.539	p^{ii}	0.495	p^i	0.440	p^{ii}	0.440
Average	0.539	Average	0.493	Average	0.439	Average	0.447

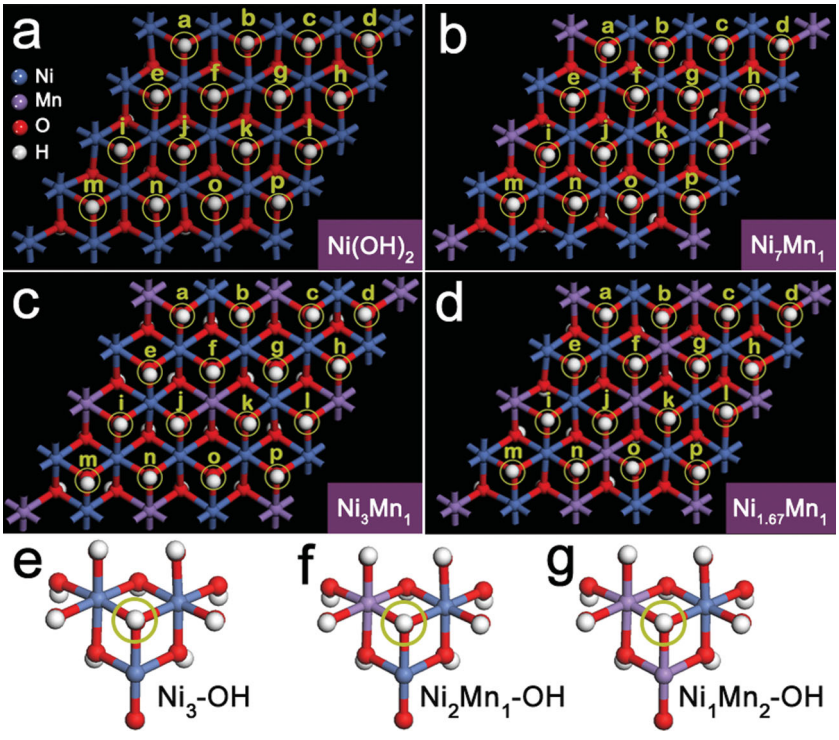

Figure 7. Optimized structures of the metal hydroxide layer for: a) $Ni(OH)_2$, b) Ni_7Mn_1-LDH, c) Ni_3Mn_1-LDH, and d) $Ni_{1.67}Mn_1$-LDH viewed along [001] direction. Three major hydroxyl groups (Ni_3–OH, Ni_2Mn_1–OH, and Ni_1Mn_2–OH) are present in (e–g).

to a high dispersion of Ni unit, improving its utilization in the Faradic energy storage.

The construction of hierarchical NiMn-LDH/CNT composites induces a simultaneous improvement in several key parameters (open accessibility, facile redox reaction and electron conduction), which can be understood by the following reasons. Firstly, the LDH offers a stable matrix for accommodating Ni and Mn unit with a well-defined and homogeneous arrangement (Figure S16, Supporting Information), allowing a refinement of electronic structure and interfacial characteristics for boosting the electrochemically active capacitance. Secondly, the direct and firm contact of NiMn-LDH nanosheets to the highly conductive CNT backbone via chemical bonding builds up an electron transfer channel and thus facilitates the reaction kinetics. Thirdly, the CNTs may serve as a structural buffer layer to the internal strain during charge-discharge cycling, owing to its mechanically robust property. In addition, the unique 3D NiMn-LDH/CNT architecture provides sufficient exposure of active centers with the interconnected mesoporous network, which enables fast ion migration and efficient redox reaction.

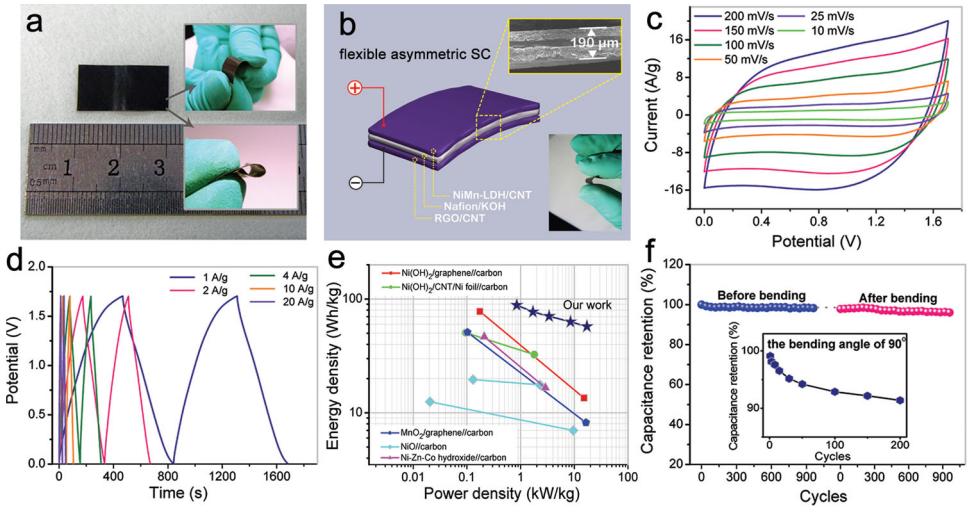

Figure 8. a) Optical photographs of the flexible NiMn-LDH/CNT film; b) schematic of the flexible asymmetric SC device based on NiMn-LDH/CNT, RGO/CNT electrode and Nafion/KOH electrolyte; c) CV curves of the device at various scan rates; d) galvanostatic charge-discharge curves of the device at various current densities; e) Ragone plots of the flexible SC, in comparison with references; f) cycling performance of the device at a current density of 10 A g^{-1} before and after bending to 90° for 100 times (inset: cycling performance with a bending angle of 90°).

2.3. Asymmetric All-Solid-State SC Device

In comparison to conventional liquid-based SCs, a solid-state flexible device offers several desirable advantages including ease of handling, scalability, flexibility, improved safety and wide operation temperature range. In this work, a flexible asymmetric SC device was fabricated by using a NiMn-LDH/CNT film as the positive electrode, a reduced graphene oxide/carbon nanotube (RGO/CNT) film as the negative electrode and the Nafion/KOH polymer as the solid electrolyte. As shown in **Figure 8**a, the NiMn-LDH/CNT film (1 cm × 2 cm, 3 mg cm^{-2}) functionalized with Nafion polymer exhibits enhanced processability and flexiblity without any cracks. In fact, a tensile strength test from a 50 μm film (76 wt% of NiMn-LDH) reveals a Young's modulus of 2.3 GPa and a tensile strength of 48 MPa, demonstrating its superior mechanical properties. In addition, the four probe measurement shows the electrical conductivity of the flexible NiMn-LDH/CNT film is typically ≈18 S cm^{-1}. Therefore, the NiMn-LDH/CNT film meets the requirements of high mechanical and electrical properties for flexible SCs. The configuration of all-solid-state flexible SC device described herein is schematically shown in Figure 8b. The total mass of the active materials on the positive and negative electrode are 3 and 18 mg, respectively, close to the optimal mass ratio based on the specific capacitance and potential range for these electrodes (Figure S17, Supporting Information).[51,52] The as-fabricated NiMn-LDH/CNT//RGO/CNT device is rather thin (thickness: ≈190 μm), light-weight (≈25 mg) and highly flexible. Figure 8c displays the CV curves of the asymmetric SC measured at the scan rate ranging in 5–200 mV s^{-1} between 0 and 1.7 V. Unlike the sharp redox peaks observed in the NiMn-LDH/CNT electrode, these CV curves exhibit nearly rectangular shape, suggesting a pseudo-constant charged/discharged rate process over the entire voltammetric cycle. The potential versus time profiles obtained by the galvanostatic charge-discharge technique at different currents (Figure 8d) show the highly linear correlation and the symmetrical shape with a quick *I*–*V* response, which also represents an ideal capacitive behavior of this SC device. The specific capacitance calculated on the basis of the total mass of the device (both positive and negative electrodes, and electrolyte) reaches to 221 F g^{-1} at a current density of 1 A/g.

The self-discharge behavior was further tested at room temperature as shown in Figure S18, Supporting Information. The device shows a stable output voltage at ≈0.9 V after 10 h; and almost 52% of the initial charged voltage was retained even after 30 h. The energy (*E*) and power densities (*P*) were calculated from galvanostatic discharge curves and plotted on the Ragone diagram (Figure 8e). The maximum energy density of 88.3 Wh kg^{-1} (at a power density of 0.85 kW kg^{-1}) and power density of 17.2 kW kg^{-1} (at a energy density of 57.1 Wh kg^{-1}) were achieved at an operating voltage of 1.7 V, superior to previously reported systems such as $Ni(OH)_2$/graphene//carbon,[51] $Ni(OH)_2$/CNT/Ni foil//carbon,[20] MnO_2/graphene//carbon,[52] NiO//carbon,[53,54] and Ni-Zn-Co hydroxide//carbon.[55] The energy density (88.3 Wh kg^{-1}) in this work, to the best of our knowledge, is the highest value reported for metal oxides/hydroxides-based asymmetric and flexible SCs. After bending to 90° for 100 times, the device still displays good long-term stability: <6% decrease after 1000 cycles (Figure 8f). The cycling performance of the device with a bending angle of 90° was also tested: 91% of its initial capacitance was retained after 200 cycles (inset of Figure 8f). By virtue of the high energy density, flexible and mechanical features, the NiMn-LDH/CNT//RGO/CNT SCs can serve as a promising power supply device in areas of miniaturized and portable/wearable electronics.

3. Conclusions

In summary, a facile in situ synthetic route has been developed to directly grow NiMn-LDH nanosheets onto the

surface of CNT backbone for SC applications. In this integrated and hierarchical configuration, the NiMn-LDH plays the role of electrochemically active species while the CNT scaffold serves as both support and electron collector. Electrochemical evaluation reveals that the unique NiMn-LDH/CNT electrode delivers a high specific capacitance (2960 F g^{-1} at 1.5 A g^{-1}) with good rate capability and excellent cycleability, which can be attributed to the synergetic contribution from the conductive CNT core and the active LDH shell. An all-solid-state flexible SC with asymmetric configuration was further fabricated based on the free-standing NiMn-LDH/CNT electrode and RGO/CNT electrode, which achieves an extremely high energy density up to 88.3 Wh kg^{-1}. These results suggest that this 3D robust nanostructure enabled by the desirable features of CNT and LDH could have significant potential as electrode materials for wearable and lightweight energy storage devices.

4. Experimental Section

Pre-Treatment of CNTs: The CNTs used in this work were synthesized by ethylene cracking on ceramic spheres through a floating catalysis process,[56] of which the diameter ranges in 30–40 nm and the length is about several micrometers. For the chemical modification of CNT surface, the CNTs (3 g) was refluxed in HNO_3 (65 wt%, 90 mL) at 120 °C for 5 h, followed by washing thoroughly with DI water, dried at 60 °C for further use.

Synthesis of the NiMn-LDH/CNT Hierarchical Structure: 10 mg of CNTs was dispersed in 250 mL of mixed metal salts solution containing $Ni(NO_3)_2{\cdot}6H_2O$, $Mn(NO_3)_2{\cdot}4H_2O$ (a total concentration of 0.006 M), and NH_4F (0.018 M) by ultra-sonication for 60 min. A second solution (60 mL) containing NaOH (0.012 M) and Na_2CO_3 (0.03 M) was added dropwise over 4 h into the above solution with vigorous stirring. The resulting suspension was aged at room temperature for 12 h. Air was bubbled throughout the entire addition period for the oxidation of Mn^{2+}. The final product was washed thoroughly and dried at room temperature. For the CoMn-LDH/CNT sample, the synthetic procedure was similar to the above method except $Co(NO_3)_2{\cdot}6H_2O$ used as the divalent metal salt. For the $Ni(OH)_2$/CNT sample, the CNTs (10 mg) was dispersed in DI water (50 mL) containing $Ni(NO_3)_2{\cdot}6H_2O$ (0.008 M), NH_4F (0.015 M) and hexamethylenetetramine (HMT; 0.05 M) by ultra-sonication for 60 min. Subsequently, the as-formed suspension was transferred into an autoclave, sealed, and heated at 90 °C for 12 h, followed by washing and drying at room temperature.

Fabrication of the NiMn-LDH/CNT//RGO/CNT SC Device: The NiMn-LDH/CNT//RGO/CNT SC device (area: 1 cm × 1 cm; total mass: 22 mg) was fabricated by assembly of a solvent-cast Nafion electrolyte membrane between the NiMn-LDH/CNT film and the RGO/CNT film face-to-face. The NiMn-LDH/CNT film was prepared by filtering the homogeneous DI water/propanol solvent (1:1, v/v) containing Nafion polymer and NiMn-LDH/CNT (1:9, w/w) through a Whatman cellulose membrane (47 mm in diameter, 0.2 μm in pore size). The obtained film was vacuum dried for 24 h and the carefully peeled off from the filter membrane. The as-prepared free-standing flexible NiMn-LDH/CNT film serves as the positive electrode for SCs. For the negative electrode, the RGO/CNT film was fabricated by the same vacuum filtration procedure (w_{Nafion}:w_{RGO}:w_{CNT} = 10:45:45). Nafion solution in *N,N*-dimethylacetamide was mixed with KOH (1 M) and stirred until the mixture became a homogeneous solution. Subsequently, the NiMn-LDH/CNT and RGO/CNT film were wetted and wrapped by the above Nafion electrolyte and pressed together. After the solidification of the electrolyte, the NiMn-LDH/CNT//RGO/CNT SC was obtained through a hot pressing procedure (50 kg cm^{-2}), resulting in close contact between the electrolyte and the electrode.

Material Characterization: X-ray diffraction (XRD) patterns were recorded by a Rigaku XRD-6000 diffractometer, using Cu-Kα radiation (0.15418 nm) at 40 kV, 30 mA. The morphology was investigated using a scanning electron microscope (SEM; Zeiss SUPRA 55) with an accelerating voltage of 20 kV, combined with energy dispersive X-ray spectroscopy (EDX). Transmission electron microscopy (TEM) images were recorded with a JEOL JEM-3010. High-resolution TEM (HRTEM) and high-angle annular dark-field scanning TEM (HAADF-STEM) images were collected on an FEI Tecnai G2 F20 S-Twin working at 200 kV. The relative energy-dispersive X-ray spectrometry (EDS) elemental mapping and line scan in the STEM was operated with a probe focused to 0.2 nm and camera length of 20 cm. X-ray photoelectron spectroscopy (XPS) measurements were performed using an ESCALAB 250 instrument (Thermo Electron) with Al Kα radiation. Raman measurements were carried out with 633 nm of excitation by using a confocal Raman microspectrometer (Renishaw, inVia-Reflex, 633 nm). Nitrogen adsorption/desorption isotherms were measured on a Quantachrome Autosorb-1CVP analyzer. The specific surface areas were calculated using the Brunauer-Emmett-Teller (BET) method. The mechanical properties of free-standing films were measured under tensile mode in a universal mechanical testing machine (Instron, FastTrack 8800 Servohydraulic Systems) with load speed of 0.5 mm/min. A CHI 660E electrochemical workstation (Shanghai Chenhua Instrument Co., China) was employed for all the electrochemical measurements. For the three-electrode configuration, a saturated Hg/HgO electrode and a platinum plate serve as the reference and counter electrode, respectively. The EIS measurement was performed by applying an AC voltage with 5 mV amplitude in a frequency range 0.01–100 kHz at open circuit voltage.

The specific capacitance of the NiMn-LDH/CNT and $Ni(OH)_2$/CNT sample was calculated from the charge–discharge curves based on the following equation:

$$C_s = \frac{I \times \Delta t}{m \times \Delta V} \tag{1}$$

where C_s (F g^{-1}) is the specific capacitance; I (A) refers to the discharge current, ΔV (V) represents the potential change within the discharge time Δt (s), and m (g) corresponds to the total weight of the NiMn-LDH (or $Ni(OH)_2$) and the CNT.

Energy density and power density of the flexible SC device were calculated using the following equations:

$$C = \frac{I \times \Delta t}{M \times \Delta V} \tag{2}$$

$$E = \frac{1}{2} \times C \times (\Delta V)^2 \tag{3}$$

$$P = \frac{E}{\Delta t} \tag{4}$$

where C (F g^{-1}) is the capacitance of the SC device; I (A) represents the discharge current; ΔV (V) refers to the potential change within the discharge time Δt (s); M (g) is the total weight of the flexible SC device; E (Wh kg^{-1}) corresponds to the energy density; P (kW kg^{-1}) is the power density.

Supporting Information

Supporting Information is available from the Wiley Online Library or from the author.

Acknowledgements

This work was supported by the 973 Program (Grant No.: 2011CBA00504), the National Natural Science Foundation of China

(NSFC), the Scientific Funds from Beijing Municipal Commission of Education (20111001002), and the Fundamental Research Funds for the Central Universities (ZD 1303). M.W. particularly appreciates the financial aid from the China National Funds for Distinguished Young Scientists of the NSFC.

Received: October 25, 2013
Revised: December 9, 2013
Published online: January 28, 2014

[1] V. L. Pushparaj, M. M. Shaijumon, A. Kumar, S. Murugesan, L. Ci, R. Vajtai, R. J. Linhardt, O. Nalamasu, P. M. Ajayan, *Proc. Natl. Acad. Sci. U. S. A.* **2007**, *104*, 13574.
[2] J. R. Miller, *Science* **2012**, *335*, 1312.
[3] M. F. El-Kady, V. Strong, S. Dubin, R. B. Kaner, *Science* **2012**, *335*, 1326.
[4] F. Meng, Y. Ding, *Adv. Mater.* **2011**, *23*, 4098.
[5] M. Beidaghi, C , Wang, *Adv. Funct. Mater.* **2012**, *22*, 4501.
[6] Y. Meng, Y. Zhang, C. Hu, H. Cheng, Y. Hu, Z. Zhang, G. Shi, L. Qu, *Adv. Mater.* **2013**, *25*, 2326.
[7] W. Chen, R. B. Rakhi, L. Hu, X. Xie, Y. Cui, H. N. Alshareef, *Nano Lett.* **2011**, *11*, 5165.
[8] J. Bae, M. K. Song, Y. J. Park, J. M. Kim, M. Liu, Z. L. Wang, *Angew. Chem. Int. Ed.* **2011**, *50*, 1683.
[9] B. G. Choi, J. Hong, W. H. Hong, P. T. Hammond, H. Park, *ACS Nano* **2011**, *5*, 7205.
[10] X. Yang, F. Zhang, L. Zhang, T. Zhang, Y. Huang, Y. Chen, *Adv. Funct. Mater.* **2013**, *23*, 3353.
[11] J. Chen, K. Sheng, P. Luo, C. Li, G. Shi, *Adv. Mater.* **2012**, *24*, 4569.
[12] P. Xu, T. Gu, Z. Cao, B. Wei, J. Yu, F. Li, J.-H. Byun, W. Lu, Q. Li, T.-W. Chou, *Adv. Energy Mater.* **2013**, DOI: 10.1002/aenm.201300759.
[13] D.-W. Wang, F. Li, J. Zhao, W. Ren, Z.-G. Chen, J. Tan, Z.-S. Wu, I. Gentle, G. Q. Lu, H.-M. Cheng, *ACS Nano* **2009**, *3*, 1745.
[14] K. Wang, Q. Meng, Y. Zhang, Z. Wei, M. Miao, *Adv. Mater.* **2012**, *25*, 1494.
[15] Y. Xu, M. G. Schwab, A. J. Strudwich, I. Henning, X. Feng, Z. Wu, K. Müllen, *Adv. Energy Mater.* **2013**, *3*, 1035.
[16] D. P. Cole, A. L. M. Reddy, M. G. Hahm, R. McCotter, A. H. C. Hart, R. Vajtai, P. M. Ajayan, S. P. Karna, M. L. Bundy, *Adv. Energy Mater.* **2013**, DOI: 10.1002/aenm.201300844.
[17] Y. Cheng, S. Lu, H. Zhang, C. V. Varanasi, J. Liu, *Nano Lett.* **2012**, *12*, 4206.
[18] R. R. Bi, X. L. Wu, F. F. Cao, L. Y. Jiang, Y. G. Guo, L. J. Wan, *J. Phys. Chem. C* **2010**, *114*, 2448.
[19] C. Yuan, L. Yang, L. Hou, J. Li, Y. Sun, X. Zhang, L. Shen, X. Lu, S. Xiong, X. W. Lou, *Adv. Funct. Mater.* **2012**, *22*, 2560.
[20] Z. Tang, C. Tang, H. Gong, *Adv. Funct. Mater.* **2012**, *22*, 1272.
[21] H. Wang, H. S. Casalongue, Y. Liang, H. Dai, **2010**, *132*, 7242.
[22] H. Jiang, P. S. Lee, C. Li, *Energy Environ. Sci.* **2012**, *6*, 41.
[23] J.-H. Kim, K. H. Lee, L. J. Overzet, G. S. Lee, *Nano Lett.* **2011**, *11*, 2611.
[24] J. Liu, J. Jiang, C. Cheng, H. Li, J. Zhang, H. Gong, H. J. Fan, *Adv. Mater.* **2011**, *23*, 2076.
[25] X.-P. Gao, H.-X. Yang, *Energy Environ. Sci.* **2010**, *3*, 174.
[26] Z. Liu, R. Ma, M. Osada, K. Takada, T. Sasaki, *J. Am. Chem. Soc.* **2005**, *127*, 13869.
[27] P. Oliva, J. Leonardi, J. F. Laurent, C. Delmas, J. J. Braconnier, M. Figlarz, F. Fievet, *J. Power Sources* **1982**, *8*, 229.
[28] L. Guerlou-Demourgues, C. Delmas, *J. Power Sources* **1994**, *52*, 275.
[29] A. Martínez, A. B. Hungría, M. Fernández-García, A. Iglesias-Juez, J. C. Conesa, G. C. Mather, G. Munuera, *J. Power Sources* **2005**, *151*, 43.
[30] C.-C. Wang, C.-C. Hu, *Electrochim. Acta* **2005**, *50*, 2573.
[31] M. Morishita, S. Ochiai, T. Kakeya, T. Ozaki, Y. Kawabe, M. Watada, S. Tanase, T. Sakai, *J. Electrochem. Soc.* **2008**, *155*, A936.
[32] C. G. Silva, Y. Bouizi, V. Fornés, H. García, *J. Am. Chem. Soc.* **2009**, *131*, 13833.
[33] J. Liang, R. Ma, N. Iyi, Y. Ebina, K. Takada, T. Sasaki, *Chem. Mater.* **2010**, *22*, 371.
[34] Q. Wang, D. O'Hare, *Chem. Rev.* **2012**, *112*, 4124.
[35] J.-H. Choy, S.-Y. Kwak, J.-S. Park, Y.-J. Jeong, J. Portier, *J. Am. Chem. Soc.* **1999**, *121*, 1399.
[36] A. M. Fogg, V. M. Green, H. G. Harvey, D. O'Hare, *Adv. Mater.* **1999**, *11*, 1466.
[37] C. Mousty, L. Vieille, S. Cosnier, *Biosens. Bioelectron.* **2007**, *22*, 1733.
[38] M. Gong, Y. Li, H. Wang, Y. Liang, J. Z. Wu, J. Zhou, J. Wang, T. Regier, F. Wei, H. Dai, *J. Am. Chem. Soc.* **2013**, *135*, 8452.
[39] H. Chen, L. Hu, M. Chen, Y. Yan, L. Wu, *Adv. Funct. Mater.* **2013**, DOI: 10.1002/adfm.201301747.
[40] M. Shao, F. Ning, J. Zhao, M. Wei, D. G. Evans, X. Duan, *Adv. Funct. Mater.* **2013**, *23*, 1733.
[41] M. A. Woo, M. S. Song, T. W. Kim, I. Y. Kim, J. Y. Ju, Y. S. Lee, S. J. Kim, J. H. Choy, S. J. Hwang, *J. Mater. Chem.* **2011**, *21*, 4286.
[42] Z.-J. Fan, J. Yan, T. Wei, G.-Q. Ning, L.-J. Zhi, J.-C. Liu, D.-X. Cao, G.-L. Wang, F. Wei, *ASC Nano* **2011**, *5*, 2787.
[43] J. Jiang, J. Liu, W. Zhou, J. Zhou, X. Huang, X. Qi, H. Zhang, T. Yu, *Energy Environ. Sci.* **2011**, *4*, 5000.
[44] W. Kagunya, R. Baddour-Hadjean, F. Kooli, W. Jones, *Chem. Phys.* **1998**, *236*, 225.
[45] R. Yuge, J. Miyawaki, T. Ichihashi, S. Kuroshima, T. Yoshitake, T. Ohkawa, Y. Aoki, S. Iijima, M. Yudasaka, *ACS Nano* **2010**, *4*, 7337.
[46] Y. J. Wei, L. Y. Yan, C. Z. Wang, X. G. Xu, F. Wu, G. Chen, *J. Phys. Chem. B* **2004**, *108*, 18547.
[47] P. Lin, Q. J. She, B. L. Hong, X. J. Liu, Y. N. Shi, Z. Shi, M. S. Zheng, Q. F. Dong, *J. Electrochem. Soc.* **2010**, *157*, A818.
[48] X. Li, J. Rong, B. Wei, *ACS Nano* **2010**, *4*, 6039.
[49] Y. Sun, Z. Sun, S. Gao, H. Cheng, Q. Liu, J. Piao, T. Yao, C. Wu, S. Hu, S. Wei, Y. Xie, *Nat. Commun.* **2012**, *3*, 1057.
[50] B. G. Choi, M. Yang, S. C. Jung, K. G. Lee, J.-G. Kim, H. Park, T. J. Park, S. B. Lee, Y.-K. Han, Y. S. Huh, *ACS Nano* **2013**, *7*, 2453.
[51] J. Yan, Z. Fan, W. Sun, G. Ning, T. Wei, Q. Zhang, R. Zhang, L. Zhi, F. Wei, *Adv. Funct. Mater.* **2012**, *22*, 2632.
[52] Z. Fan, J. Yan, T. Wei, L. Zhi, G. Ning, T. Li, F. Wei, *Adv. Funct. Mater.* **2011**, *21*, 2366.
[53] D. W. Wang, F. Li, H. M. Cheng, *J. Power Sources* **2008**, *185*, 1563.
[54] H. Inoue, Y. Namba, E. Higuchi, *J. Power Sources* **2010**, *195*, 6239.
[55] H. Wang, Q. Gao, J. Hu, *J. Power Sources* **2010**, *195*, 3017.
[56] Q. Zhang, J.-Q. Huang, M.-Q. Zhao, W.-Z. Qian, Y. Wang, F. Wei, *Carbon* **2008**, *46*, 1152.